

# Altitude-Adaptive Vision-Only Geo-Localization for UAVs in GPS-Denied Environments

Xingyu Shao<sup>1</sup>, Mengfan He<sup>1</sup>, Chunyu Li<sup>1</sup>, Liangzheng Sun<sup>1</sup> and Ziyang Meng<sup>1</sup>, *Senior Member, IEEE*

**Abstract**—To address the scale mismatch caused by large altitude variations in UAV visual place recognition, we propose a monocular vision-only altitude-adaptive geo-localization framework. The method first estimates relative altitude from a single downward-looking image by transforming the input into the frequency domain and formulating altitude estimation as a regression-as-classification (RAC) problem. The estimated altitude is then used to crop the query image to a canonical scale, after which a classification-then-retrieval visual place recognition module performs coarse localization. To improve retrieval robustness under varying image quality, we further introduce a quality-adaptive margin classifier (QAMC) and refine the final location by weighted coordinate estimation over the top retrieved candidates. Experiments on two synthetic datasets and two real-flight datasets show that the relative altitude estimation (RAE) module yields clear overall improvements in downstream retrieval performance under significant altitude changes. With our visual place recognition module, altitude adaptation improves average R@1 and R@5 by 41.50 and 56.83 percentage points, respectively, compared with using the same retrieval pipeline without altitude normalization, and the full system runs at 13.3 frames/s on the reported workstation hardware. These results indicate that relative altitude estimation provides an effective scale prior for cross-altitude UAV geo-localization and supports GPS-denied coarse initialization without auxiliary range sensors or topological inputs.

**Index Terms**—Visual Place Recognition (VPR), Airborne Platforms, Relative Altitude Estimation, Coarse Localization, Plug-and-Play Solution, Unmanned Aerial Vehicle (UAV)

## I. INTRODUCTION

UNMANNED aerial vehicles (UAVs) are increasingly used in intelligent transportation systems for tasks such as traffic monitoring, transportation-corridor inspection, and low-altitude logistics. In GPS-denied environments, visual place recognition (VPR) functions as a localization mechanism for autonomous navigation. A primary characteristic of airborne VPR, compared with ground-based systems, is altitude variation. Dynamic altitude variations induce scale discrepancies in downward-looking imagery, which affect the

This work was supported in part by a grant of the National Nature Science Foundation of China under Grant 62403269. (*Corresponding author: Ziyang Meng.*)

Xingyu Shao, Mengfan He and Ziyang Meng are with the Department of Precision Instrument, Tsinghua University, Beijing 100084, China (e-mail: shao-xy21@mails.tsinghua.edu.cn; hmf21@mails.tsinghua.edu.cn; ziyangmeng@tsinghua.edu.cn).

Chunyu Li was with the Department of Precision Instrument, Tsinghua University, Beijing 100084, China. He is now with the School of Aerospace Engineering, Beijing Institute of Technology, Beijing 100081, China (e-mail: chunyu@bit.edu.cn).

Liangzheng Sun is with the School of Instrumentation Science and Optoelectronics Engineering, Beijing Information Science and Technology University, Beijing 100192, China (e-mail: 2023030031@bistu.edu.cn).

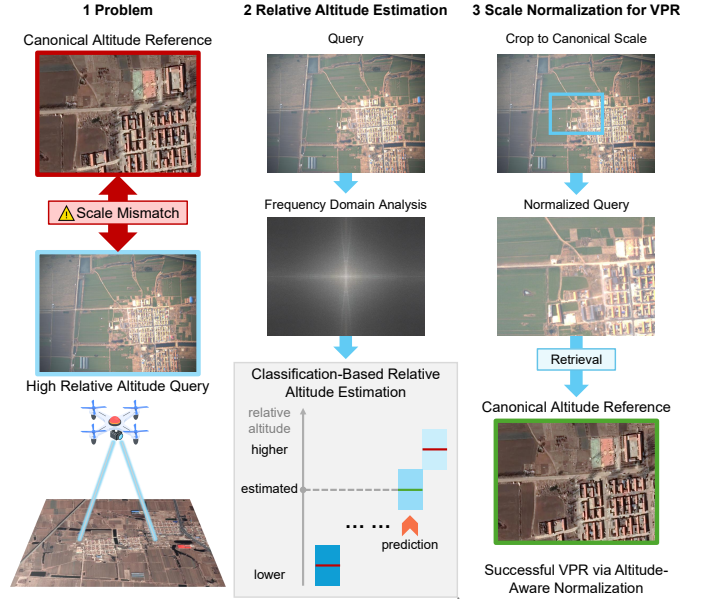


Fig. 1. The overview of the proposed method: altitude variation causes scale mismatch, while frequency-domain altitude estimation and altitude-aware cropping normalize the query image to a canonical scale for more reliable cross-altitude VPR.

performance of VPR methods predicated on fixed-scale assumptions. Therefore, aligning the observation scale between query images and the reference database is an important step for reliable geo-initialization.

Conventional aerial platforms typically estimate altitude using barometric measurements, digital elevation model (DEM) alignment, or time-of-flight (ToF) sensors. However, barometric measurements provide pressure-referenced altitude rather than altitude above ground level (AGL). Recovering AGL further requires reliable terrain elevation at the current position, which may be unavailable during GPS-denied initialization, and barometric measurements themselves are also affected by atmospheric fluctuations. DEM-based solutions are likewise limited in unmapped or weakly mapped regions. Direct time-of-flight (dToF) sensors can provide metric distance measurements, but their size, weight, and power (SWaP) demands may exceed the payload constraints of small- to medium-sized UAVs. Consequently, vision-based altitude estimation presents an attractive alternative. Although monocular metric depth estimation (MMDE) models have advanced significantly, they are primarily optimized for near-field, pixel-wise depth prediction using localized textures. For UAVs operating at altitudes of hundreds of meters, the near-nadir view and the

reduced fine-grained geometric details introduce substantial domain shifts, which limit the direct applicability of these dense regression models to global relative-altitude approximation.

As illustrated in Fig. 1, relative altitude variation causes scale mismatch between the query and the canonical reference map. To address this, we propose an altitude-adaptive geo-localization system for airborne platforms. Our objective is not to recover a highly precise continuous altitude value per se, but to estimate a robust scale prior for altitude-guided query normalization. The mapping from high-altitude monocular imagery to physical altitude is highly nonlinear, and neighboring altitudes can exhibit ambiguous visual cues when training relies primarily on resampled satellite imagery under a synthetic-to-real gap. These properties make interval-level prediction more suitable than direct point regression in our setting; in preliminary trials, direct continuous regression objectives were also less stable to optimize. Accordingly, we transform spatial-domain images into the frequency domain via a two-dimensional fast Fourier transform and formulate altitude estimation as a discrete classification task over pre-defined bins. By integrating a fixed-interval regression-as-classification (RAC) strategy, the system provides a scale prior to compensate for nonlinear scale variations. The estimated altitude guides the cropping of query images into normalized primitive views, which are subsequently integrated into a classification-based VPR pipeline. To handle image-quality variations, we introduce a quality-adaptive margin classifier (QAMC) that modulates the decision margin based on image sharpness. Finally, after retrieving the top- $N$  database candidates, a weighted coordinate estimation (WCE) module is employed to refine the coarse cell-based predictions into sub-grid coordinate estimates.

The proposed plug-and-play framework requires no additional hardware and provides a visual geo-initialization module for UAVs. Our key contributions are summarized as follows:

- We propose a single-image vision-only geo-localization framework for UAVs that adapts to altitude variations through relative-altitude estimation and altitude-guided query normalization. By translating spatial-domain images into frequency-domain representations and reframing the regression problem into a classification task with a discretized binning strategy, the altitude estimation module provides a stable scale prior from a single nadir image.
- We introduce a quality-adaptive margin classifier (QAMC) to extract discriminative embeddings from aerial inputs of varying clarity. To derive specific geographic locations from the retrieval results, a weighted coordinate estimation (WCE) strategy is applied to the top- $N$  retrieved candidates, mitigating the quantization errors inherent in coarse grid partitioning and achieving sub-grid coordinate recovery.
- We demonstrate the feasibility of the proposed pipeline through evaluations on both real-flight datasets and synthetic datasets derived from satellite imagery, encompassing diverse rural and semi-urban terrains. The system achieves an inference speed of 13.3 FPS on the reported

workstation hardware, operating without reliance on temporal multi-frame sequences, specific semantic targets, or auxiliary distance sensors.

The remainder of this paper is organized as follows. Section II reviews related works on aerial visual place recognition, vision-based UAV altitude estimation, and regression-as-classification. Section III presents the proposed altitude-adaptive geo-localization framework, including the relative altitude estimation module and the visual place recognition module. Section IV describes the datasets, experimental settings, main results, runtime analysis, and ablation studies. Section V discusses scalability, limitations, and potential directions for future work. Finally, Section VI concludes the paper.

## II. RELATED WORKS

This section reviews the literature pertinent to the proposed system, focusing on the evolution of VPR for airborne platforms, vision-based altitude estimation techniques, and the theoretical foundations of frequency-domain representation and regression-as-classification.

### A. VPR for Airborne Platforms and Scale Discrepancy

Visual place recognition (VPR) has been extensively studied for ground-based navigation and geo-localization. Traditionally, VPR is formulated as an image retrieval task, in which global descriptors are extracted from query and reference images and matched against a pre-constructed database [1], [2]. However, applying these retrieval-based pipelines to airborne platforms (e.g., UAVs) introduces distinct geometric challenges. Unlike ground vehicles with relatively stable camera-to-ground distance, UAVs operate with high three-dimensional mobility. The resulting altitude variations induce scale discrepancies and viewpoint changes, which degrade retrieval robustness when query and reference images are captured at different flight altitudes.

Beyond retrieval-based pipelines, recent advances have also explored classification-based formulations for large-scale visual geo-localization and VPR. Approaches such as PlaNet [3], CPlaNet [4], and CosPlace [5] formulate localization by discretizing geographic space into cells and learning place-specific prototypes or classification targets. Building upon this, Divide & Classify (D&C) [6] partitions regions into uniform UTM grids and employs angular margin losses to match features to spatial prototypes. More recently, EigenPlaces [7] improved viewpoint robustness through a training protocol that explicitly groups different views of the same place during representation learning. For UAV-specific applications, GeoVINS [8] incorporated a classify-then-retrieve geo-localization stage into a broader aerial visual-inertial framework. While effective, most of these frameworks assume a fixed or weakly varying operational altitude and do not explicitly compensate for the continuous scale variations caused by vertical UAV maneuvers.

### B. Vision-based UAV Altitude Estimation

Compensating for scale discrepancies requires estimating the relative altitude or metric scale from UAV imagery. Representative altitude- and scale-related methods most relevant

to our setting are summarized in Table I. Earlier vision-based studies also explored altitude inference from monocular aerial imagery. Cherian et al. [9] estimated UAV altitude from top-down images captured by a single onboard camera using texture-based learning with temporal refinement. Campos et al. [10] addressed terrain-following altitude estimation from monocular video by combining optical flow, motion information from the UAV flight controller, and a decision-tree-based reliability classifier. More broadly, geometric approaches rely on stereoscopic vision or sequential frame analysis. Stereoscopic systems compute altitude or scale cues from calibrated multi-camera geometry, either through disparity or, as in mixed fish-eye/perspective rigs, through ground-plane homography and plane sweeping [11], while sequence-based methods employ optical flow or structure-from-motion (SfM) to derive relative scale from temporal trajectories [12]. Although these methods provide geometric constraints, their performance inherently depends on temporal consistency or strict hardware calibration, which can be interrupted during aggressive UAV maneuvers or irregular frame sampling. These studies demonstrate the feasibility of vision-based altitude inference, but they are not designed as scale-prior modules for altitude-adaptive aerial VPR.

A recent deep-learning-based nadir-image study by Arık [13] trains a ResNet50 regressor on large-scale real-flight UAV imagery, with AGL labels derived from EXIF-based GPS altitude and DEM subtraction. Although this setting is closer to ours in terms of monocular nadir imagery, it remains a direct altitude-regression framework trained on target-domain real flight data and does not use the estimated altitude as a scale prior for downstream altitude-adaptive aerial VPR. Alternatively, semantic-anchor-based approaches leverage the physical dimensions of known objects as scale cues. For instance, a recent scale-aware geo-localization framework [14] utilizes detected small vehicles as semantic anchors and infers absolute metric scale through a decoupled stereoscopic projection model. This approach is more suitable for urban environments where such semantic anchors are sufficiently visible. However, its direct applicability is constrained in unstructured terrains (e.g., agricultural fields or forests) where predefined semantic targets are sparse or absent. Our system, in contrast, estimates relative altitude from a single downward-looking image based on frequency-domain global structural density, operating independently of temporal multi-frame cues, stereo geometry, and specific semantic bounding boxes, and is trained using synthetic multi-altitude samples generated from satellite imagery rather than target-domain real flight images.

### C. Monocular Depth Baselines and Regression-as-Classification

In the absence of a closely matched baseline that estimates a global relative-altitude prior from a single nadir image under our training setting, general-purpose monocular metric depth estimation (MMDE) models serve as the closest contextual references. Foundation models such as Depth Anything V2 [15] and UniDepth V2 [16] are deployed zero-shot across diverse scenarios. These models are primarily designed for dense

metric depth prediction at the pixel level, typically in near-field visual settings. When applied zero-shot to high-altitude nadir images with limited dense local texture cues, the domain shift restricts their ability to approximate a reliable global relative-altitude prior. Furthermore, in our setting, applying direct continuous regression to texture-degraded aerial patterns can lead to less stable optimization, as the mapping between spatial appearance and continuous metric scale is highly nonlinear.

To improve robustness under this setting, our framework leverages frequency-domain analysis and regression-as-classification (RAC). Rather than relying exclusively on spatial-domain convolutions, the proposed altitude estimation module transforms the input into the frequency domain via fast Fourier transform (Spat2Freq). Studies [17], [18] indicate that frequency-domain representations can capture global structural periodicities and may be less sensitive to spatial texture degradation.

In parallel, we reformulate continuous altitude estimation as a discrete classification task. Prior studies on regression-as-classification, ordinal learning, and depth discretization [19]–[21] suggest that discretized classification losses can provide an effective alternative to direct point regression for continuous or ordinal targets, while allowing neighboring bins to encode target adjacency. In our setting, RAC yields a probability distribution over neighboring altitude bins, which naturally captures interval-level uncertainty and can lead to more stable optimization in visually ambiguous nadir imagery. By integrating a fixed-interval regression-as-classification strategy, the system outputs an interval-level altitude estimate that serves as a stable scale prior for downstream altitude-guided query normalization and altitude-adaptive aerial VPR.

## III. METHODOLOGY

We formulate the target task as an aerial VPR problem under unknown and variable flight altitudes. Given a query image  $I_{\text{in}}$  captured by an airborne platform at an unknown altitude, the goal is to estimate its relative altitude and retrieve the corresponding map tiles from a geo-referenced database constructed at a normalized altitude.

As illustrated in Fig. 2, the proposed framework consists of two core modules: a relative altitude estimation module and a VPR module, which jointly process  $I_{\text{in}}$  in a two-stage pipeline. The altitude estimation module infers the airborne platform’s relative altitude  $H$  as  $\hat{H}$ . This estimation guides an altitude-adaptive cropping of  $I_{\text{in}}$  to align its spatial scale with the reference map tiles. The VPR module then retrieves candidate reference images via a classification-based retrieval pipeline, denoted as AVPR. Formally, the process is defined by the following operations:

$$\hat{H} = (\text{Class2Alt} \circ \text{AC} \circ \text{Spat2Freq})(I_{\text{in}}), \quad (1)$$

and

$$(\mathcal{V}, \mathcal{U}) = (\text{AVPR} \circ \text{Crop})(I_{\text{in}}, \hat{H}), \quad (2)$$

where  $\mathcal{V} = \{d_i \in \mathbb{R}^d\}_{i=1}^{n_{\text{retrieve}}}$  denotes the set of retrieved global feature vectors of dimension  $d$ , and  $\mathcal{U} = \{(e_i, n_i)\}_{i=1}^{n_{\text{retrieve}}}$  represents their corresponding UTM geospatial coordinates.

TABLE I  
COMPARISON OF REPRESENTATIVE ALTITUDE- AND SCALE-RELATED METHODS FOR UAV IMAGERY AND THE PROPOSED FRAMEWORK. REPORTED OPERATING RANGES ARE LISTED ONLY WHEN EXPLICITLY STATED OR DIRECTLY INFERABLE FROM THE ORIGINAL PAPERS.

| Method             | Target output                             | Scale / altitude cue   | Additional sensor, geometry prior, or temporal dependency     | Training data source  | Reported operating range   | Designed for altitude-adaptive aerial VPR |
|--------------------|---|--|---|---|--|---|
| Cherian et al. [9] | altitude                                  | top-down texture cue   | single camera; temporal refinement                            | single-camera onboard aerial imagery  | not explicitly reported; low-altitude laboratory setting   | no  |
| Campos et al. [10] | AGL altitude / terrain-following altitude | optical flow + motion information  | temporal multi-frame + flight-controller motion information   | primarily not learning-based; monocular flight videos with synchronized telemetry                           | simulation: fixed ASL 500 m above runway and fixed AGL 200 m; field: fixed AGL 25 m and low-altitude LiDAR-validated flights | no  |
| Eynard et al. [11] | altitude                                  | mixed stereo + ground-plane homography + plane sweeping                  | mixed stereo; auxiliary attitude from fisheye vision or IMU   | not learning-based; calibrated mixed stereo sequences   | ~2.2–5.1 m in mast-based tests; ~0.55–2.15 m in UAV landing/takeoff tests  | no  |
| Ye et al. [14]     | absolute metric scale                     | small-vehicle semantic anchors + decoupled stereoscopic projection model | camera intrinsics + pitch angle prior; no temporal dependency | not learning-based scale model; SV detector trained on VSAI, CVGL backbone trained on DenseUAV training set | DenseUAV+: 80–100 m; UAV-VisLoc+: 325–595 m  | no  |
| Ours               | relative altitude (AGL)                   | frequency-domain global structural density                               | nominal camera intrinsics; no temporal dependency             | synthetic multi-altitude samples generated from satellite imagery   | train: 100–700 m; test: 100–700 m (synthetic), 100–650 m (real-flight)   | yes                                       |

Before detailing the mathematical formulation of each operator, representative query samples across different datasets are presented in Fig. 3 to provide an intuitive visualization of the spatial-to-frequency transformation and the cropping process. For the relative altitude estimation module, we first introduce the image preprocessing technique Spat2Freq in Section III-A1, followed by the altitude classification operation AC and the class-to-altitude mapping function Class2Alt in Section III-A2. For the VPR module, Section III-B1 presents the primitive image extraction method Crop, and Section III-B2 details the classification-based retrieval process AVPR, including the quality-adaptive margin classifier (QAMC). By reformulating relative altitude estimation as a classification problem, the estimated altitude provides a scale prior to guide the cropping operation, thereby normalizing query images for cross-altitude retrieval.

#### A. Relative Altitude Estimation Module

The relative altitude estimation module infers the approximate relative altitude above ground level (AGL) from a single downward-looking image. Because the framework is primarily trained on resampled satellite imagery, which lacks continuous optical degradation cues present in physical flight, continuous distance regression becomes an ill-posed optimization problem. Therefore, we utilize the regression-as-classification (RAC) paradigm, estimating discrete altitude bins using frequency-domain representations.

1) *Image Pre-processing (Spat2Freq)*: In regions where ground features are sparse, spatial-domain images exhibit limited structural variations under altitude changes. Conversely, the density of frequency-domain components demonstrates

higher sensitivity to scale variations. Thus, we apply a two-dimensional fast Fourier transform (2D-FFT) to the spatial image before feeding it into the feature extractor.

Let the three channels of the input RGB image  $I_{in}$  of size  $H_I \times W_I$  be denoted by  $I_c(x, y)$ , where  $c \in \{R, G, B\}$  and  $(x, y)$  are the spatial pixel coordinates. To center the zero-frequency (DC) component in the resulting spectrum, we apply a spatial shift prior to the transform:

$$\hat{I}_c(x, y) = I_c(x, y) \cdot (-1)^{x+y}. \quad (3)$$

The centered 2D-FFT is then applied to each shifted channel:

$$F_c(u, v) = \mathcal{F}(\hat{I}_c(x, y)), \quad c \in \{R, G, B\}, \quad (4)$$

where  $\mathcal{F}$  represents the discrete Fourier transform operator, and  $(u, v)$  denote the frequency coordinates. The magnitude spectrum is computed as:

$$M_c(u, v) = |F_c(u, v)|, \quad c \in \{R, G, B\}. \quad (5)$$

To compress the high dynamic range of the spectrum coefficients, a logarithmic transformation is applied:

$$L_c(u, v) = \log_b(1 + M_c(u, v)), \quad c \in \{R, G, B\}, \quad (6)$$

where  $b$  is a predefined hyperparameter. The transformed matrices are concatenated to form the pseudo-color frequency image  $I_{in}^{\text{freq}}$ , defined by:

$$I_{in}^{\text{freq}} = [L_R, L_G, L_B] = \text{Spat2Freq}(I_{in}). \quad (7)$$

#### 2) Altitude Class Division and Network Architecture:

To formulate altitude estimation as a classification task, the continuous flight altitude range  $[H_{\min}, H_{\max})$  is uniformly discretized into  $n$  intervals with step size  $\Delta H$ . Each interval

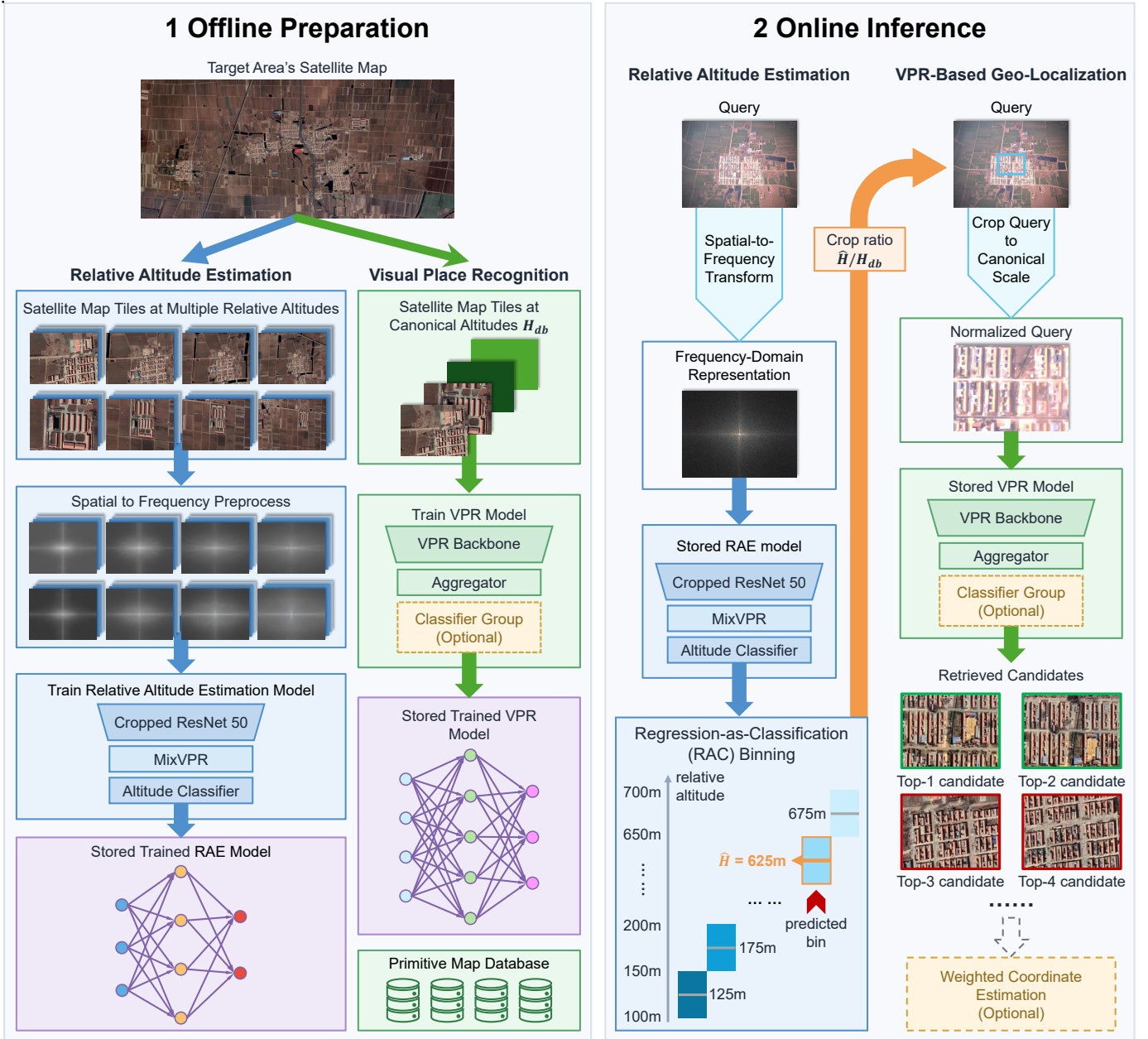


Fig. 2. Overview of the proposed altitude-adaptive geo-localization framework. The framework consists of two stages: offline preparation and online inference. During offline preparation, satellite map tiles cropped at multiple altitudes are transformed into frequency-domain samples to train the relative altitude estimation (RAE) model, while tiles cropped at the canonical altitude  $H_{ab}$  are used to train the visual place recognition (VPR) model and prepare the reference database. During online inference, a query image is first transformed into the frequency domain and fed into the stored RAE model, which predicts a relative-altitude bin through regression-as-classification (RAC). The estimated altitude is then used to crop the query to the canonical scale, producing a normalized query for the stored VPR model. The VPR model retrieves the top candidate references, and an optional weighted coordinate estimation module can be further applied to refine the final geo-location.

corresponds to an altitude class  $C_i$ . The  $i$ -th class interval is defined as:

$$C_i = \{H \mid H_{\min} + (i-1)\Delta H \leq H < H_{\min} + i\Delta H\}. \quad (8)$$

In the main experiments, we set the interval size to  $\Delta H = 50$  m. For a given altitude  $H \in [H_{\min}, H_{\max})$ , the corresponding target class index  $i^*$  is determined by:

$$i^* = \left\lfloor \frac{H - H_{\min}}{\Delta H} \right\rfloor + 1, \quad H \in [H_{\min}, H_{\max}). \quad (9)$$

The center altitude of the  $i$ -th class is given by  $H_{\text{center}}^{(i)} = H_{\min} + (i-0.5)\Delta H$ , and let  $\mathcal{H}_{\text{center}} = \{H_{\text{center}}^{(i)}\}_{i=1}^n$  denote the set of all altitude-bin center altitudes. The mapping from a predicted class index to its representative physical altitude, denoted by  $\text{Class2Alt} : \{1, \dots, n\} \rightarrow \mathcal{H}_{\text{center}}$ , is defined as:

$$\text{Class2Alt}(i) = H_{\text{center}}^{(i)}, \quad i \in \{1, \dots, n\}. \quad (10)$$

The altitude classifier, denoted by AC, processes  $I_{\text{in}}^{\text{freq}}$  and outputs an altitude-class probability vector  $p_h \in [0, 1]^n$ . We utilize the MixVPR architecture [2] to extract a global

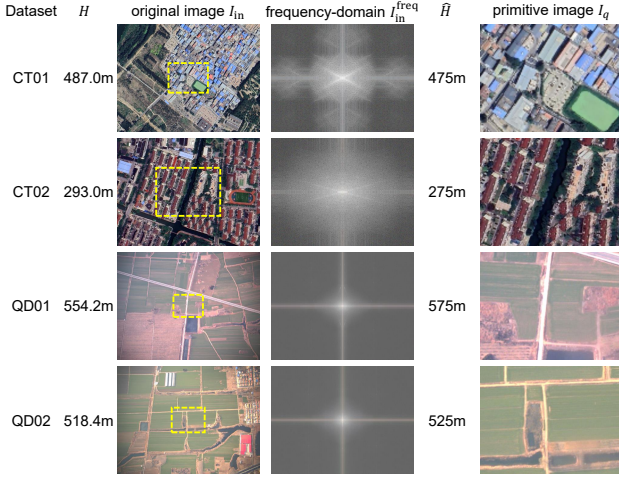


Fig. 3. Examples of raw query images, frequency-domain representations, and primitive images from the four datasets. For visual clarity, the displayed frequency-domain images are brightness-adjusted.

frequency embedding  $x_h \in \mathbb{R}^{d_h}$  from  $I_{in}^{\text{freq}}$ . Let  $W_h \in \mathbb{R}^{n \times d_h}$  denote the prototype matrix of the altitude classifier. The predicted probability of the  $i$ -th altitude class is given by:

$$p_h(i) = [\text{softmax}(W_h x_h)]_i, \quad i \in \{1, \dots, n\}. \quad (11)$$

The predicted class index is  $\hat{i} = \arg \max_{i \in \{1, \dots, n\}} p_h(i)$ . Accordingly, we define the relative altitude classification mapping  $\text{AltClassify} : \mathbb{R}^n \rightarrow \mathcal{H}_{\text{center}}$ , which outputs the estimated altitude  $\hat{H}$  by mapping  $\hat{i}$  to its corresponding center altitude:

$$\hat{H} = \text{AltClassify}(p_h) = \text{Class2Alt}(\hat{i}). \quad (12)$$

3) *Data Preparation Constraints*: During training, the ground footprint is calculated based on fixed camera intrinsics. Training samples are generated by sampling satellite imagery of the target area at uniform altitude intervals and cropping each tile to match the computed ground coverage at that altitude. At inference time, if the deployed camera's intrinsic parameters differ from the nominal parameters used during offline synthesis, the estimated altitude  $\hat{H}$  can be linearly scaled by the ratio of the physical focal lengths.

## B. VPR Module

1) *Primitive Image Collection (Crop)*: To normalize the scale discrepancy prior to feature retrieval, the input image is center-cropped to simulate a view captured at a predefined canonical altitude  $H_{\text{db}}$  centered at the same nadir point. The reference database is uniformly constructed using pre-rendered views at this specific altitude, termed the primitive map.

Let  $res_w$  and  $res_h$  denote the image width and height in pixels, and let  $f_x$  and  $f_y$  represent the focal lengths in pixels along the respective axes. Under a downward-looking pinhole camera model, the physical dimensions of the ground footprint  $W_{\text{ground}} \times H_{\text{ground}}$  captured at altitude  $H$  are:

$$W_{\text{ground}} = \frac{res_w}{f_x} \cdot H, \quad H_{\text{ground}} = \frac{res_h}{f_y} \cdot H. \quad (13)$$

To ensure that cropping does not introduce blank-edge artifacts,  $H_{\text{db}}$  must satisfy  $H_{\text{db}} \leq \min \mathcal{H}_{\text{center}}$ . To normalize the

spatial scale, the input image  $I_{in}$  is resized by a factor of  $\hat{H}/H_{\text{db}}$  and subsequently center-cropped to its original pixel dimensions ( $res_w \times res_h$ ). This scale-normalization operation is defined as the Crop function, yielding the primitive query image  $I_q$ , given by

$$I_q = \text{Crop}(I_{in}, \hat{H}). \quad (14)$$

Aligning the query image with primitive map tiles built at a fixed altitude  $H_{\text{db}}$  normalizes scale variation and enables accurate geo-initialization on memory-constrained UAVs (see Fig. 4).

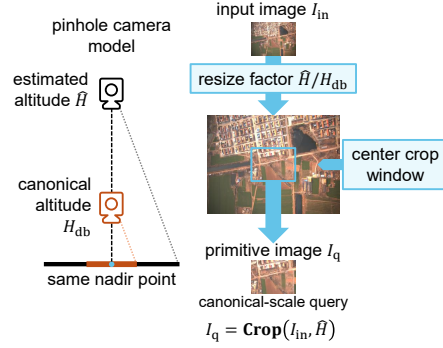


Fig. 4. Transformation from an input image to the primitive image at the canonical altitude.

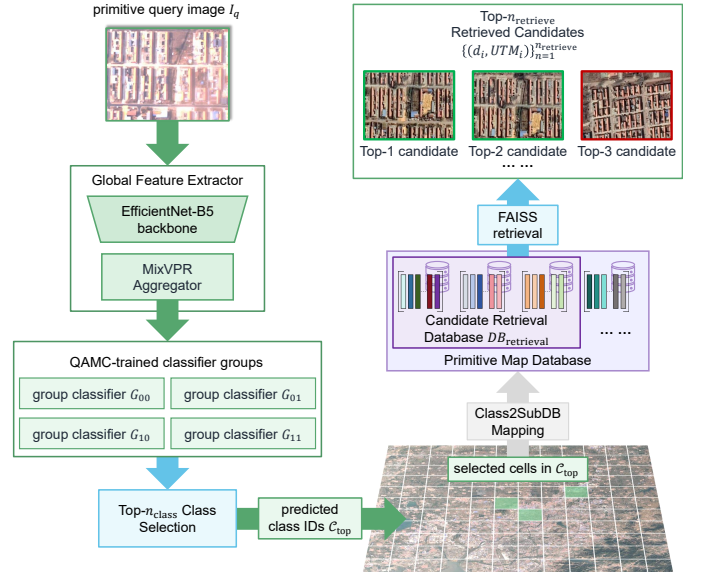


Fig. 5. Classification-then-retrieval pipeline for the primitive query image. The primitive query image  $I_q$  is encoded by an EfficientNet-B5 backbone and a MixVPR aggregator. Group-wise classifiers trained with the quality-adaptive margin classifier (QAMC) produce class scores over the spatial groups, from which the top  $n_{\text{class}}$  predicted classes  $C_{\text{top}}$  are selected. Their corresponding sub-databases are merged into the candidate retrieval database  $DB_{\text{retrieval}}$ , where feature retrieval returns the top  $n_{\text{retrieve}}$  reference descriptors and their associated UTM coordinates.

2) *Primitive Map Retrieval with Quality-Adaptive Margins*: The overall VPR pipeline is illustrated in Fig. 5. The retrieval pipeline, denoted as AVPR, follows a classify-then-retrieve strategy over the primitive map. The satellite map is partitioned into non-overlapping uniform square cells of side length  $M$ .

Each cell acts as a geographical class  $C_{e_i, n_j}$ , identified by its UTM indices:

$$C_{e_i, n_j} = \left\{ (e, n) : \left\lfloor \frac{e}{M} \right\rfloor = e_i, \left\lfloor \frac{n}{M} \right\rfloor = n_j \right\}. \quad (15)$$

To prevent perceptual aliasing and ensure rotational robustness during training, images are augmented through rotations of  $30^\circ$ , forming the augmentation set  $\alpha_{aug} = \{0, 30, \dots, 330\}$ . Furthermore, adjacent cells are dispersed into  $|G| = N^2$  disjoint groups via a modulo operation on the indices, denoted as  $G_{u,v}$  where  $u = e_i \bmod N$  and  $v = n_j \bmod N$ . The association between each geographical class and its corresponding sub-database  $DB_{e_i, n_j}$  is defined by the mapping function Class2SubDB:

$$\text{Class2SubDB} : C_{e_i, n_j} \mapsto DB_{e_i, n_j}. \quad (16)$$

To dynamically modulate the classification learning objective according to the clarity of structural details, we introduce the quality-adaptive margin classifier (QAMC), which builds upon the AdaFace loss paradigm [22]. Unlike the original AdaFace, which solely relies on the embedding norm (denoted here as  $Q_{\text{norm}}$ ) as a proxy for image quality, our QAMC further incorporates a sharpness-based indicator that explicitly measures the clarity of structural details in aerial images. Let  $I_q(x, y, c)$  denote the pixel intensity of the normalized primitive query image at spatial coordinates  $(x, y)$  for the  $c$ -th channel, where  $C = 3$  is the total number of color channels. The image is first converted to grayscale  $I_g$ :

$$I_g(x, y) = \frac{1}{C} \sum_{c=1}^C I_q(x, y, c), \quad (x, y) \in [1, res_h] \times [1, res_w]. \quad (17)$$

Given the grayscale input  $I_g$ , the edge response is computed using the Laplacian operator as  $L(x, y) = \nabla^2 I_g(x, y)$ . The sharpness score  $Q_{\text{sharp}}$  is defined as the spatial variance of  $L$ :

$$Q_{\text{sharp}} = \frac{1}{res_h res_w} \sum_{x=1}^{res_h} \sum_{y=1}^{res_w} (L(x, y) - \bar{L})^2, \quad (18)$$

where  $\bar{L}$  is the mean Laplacian response. We replace the original norm-based quality indicator with a composite quality factor  $Q$ , which combines the normalized sharpness  $\hat{Q}_{\text{sharp}}$  and the feature embedding norm  $Q_{\text{norm}}$ :

$$Q = \alpha \cdot Q_{\text{norm}} + (1 - \alpha) \cdot \hat{Q}_{\text{sharp}}, \quad \alpha \in [0, 1]. \quad (19)$$

This composite factor  $Q$  dynamically scales the angular margin in the cross-entropy loss, ensuring that images with richer structural textures enforce stricter discriminative constraints.

During inference, feature extraction is realized using the EfficientNet backbone [23] integrated with the aggregation module from MixVPR, computing a global descriptor  $x \in \mathbb{R}^d$  for  $I_q$ . For the  $k$ -th group ( $k \in \{1, \dots, |G|\}$ ), the mixture-of-experts classifier employs a prototype matrix  $W_k \in \mathbb{R}^{S_k \times d}$ , where  $S_k$  is the number of spatial classes in group  $k$ . The group-wise probability scores  $p_k(c)$  for each class  $c$  are computed as:

$$p_k(c) = [\text{softmax}(W_k x)]_c, \quad c \in \{1, \dots, S_k\}. \quad (20)$$

The QAMC modulates the decision boundary during training. During inference, we select the top  $n_{\text{class}}$  cells with the highest confidence globally:

$$C_{\text{top}} = \text{TopK}_{n_{\text{class}}} \left\{ p_k(c) \right\}_{\substack{k \in \{1, \dots, |G|\}, \\ c \in \{1, \dots, S_k\}}}, \quad (21)$$

where  $\text{TopK}_n\{\mathcal{S}\}$  denotes the mathematical operator that extracts the subset of  $n$  elements from set  $\mathcal{S}$  possessing the maximum numerical values. In our implementation, we set  $n_{\text{class}} = 3$  and  $n_{\text{retrieve}} = 10$ . The final reference database  $DB_{\text{retrieval}}$  is constructed by taking the union of the sub-databases corresponding to the selected classes in  $C_{\text{top}}$ :

$$DB_{\text{retrieval}} = \bigcup_{c \in C_{\text{top}}} \text{Class2SubDB}(c). \quad (22)$$

A feature-level similarity search is executed within  $DB_{\text{retrieval}}$  using the FAISS library [24], and the system successfully returns the top  $n_{\text{retrieve}}$  reference global features  $\mathcal{V}$  and their associated metric coordinates  $\mathcal{U}$ , concluding the visual location recall process. We formalize the AVPR pipeline as a mapping from the input image to its retrieved references and their locations:

$$(\mathcal{V}, \mathcal{U}) = \text{AVPR}(I_q). \quad (23)$$

## IV. EXPERIMENTS

### A. Dataset

While several UAV-based VPR datasets exist, they generally do not align with the specific constraints of our task. For instance, SUES-200 [25] and DenseUAV [26] are primarily constrained to low, discrete flight altitudes (typically below 300 m). Cross-view datasets such as University-1652 [27] predominantly feature target-centric oblique drone perspectives rather than continuous nadir-view mapping. Furthermore, although datasets like UAV-VisLoc [28] provide high-altitude nadir imagery with metric annotations, their flight trajectories maintain a relatively constant altitude within each dataset sequence, lacking the continuous and substantial scale dynamics required to evaluate altitude-adaptive localization. To address the scarcity of datasets featuring monocular, downward-looking imagery with large altitude variation (e.g., 100–700 m) and precise geospatial ground truth, we constructed two synthetic datasets (CT01 and CT02) and collected two real-flight datasets (QD01 and QD02) using UAV-acquired top-down imagery in rural areas of Qingdao, China. For synthetic data generation, all multi-altitude tiles are rendered under a fixed nominal pinhole camera model. Real-flight evaluation uses the corresponding nominal intrinsics unless otherwise stated, and deployment-time intrinsic mismatch is handled by focal-length-ratio scaling as described in Section III-A3.

The CT01 and CT02 datasets are synthetic and are generated by altitude-conditioned cropping of satellite maps. Under the flat-ground assumption, high-altitude near-nadir satellite maps exhibit minimal perspective distortion and can be approximated as a zero-altitude reference plane. Under fixed camera intrinsics, the ground footprint of a nadir-view pinhole camera is directly proportional to the relative altitude. We therefore compute the footprint corresponding to each target altitude

TABLE II  
SPECIFICATIONS OF THE UAV-MOUNTED SENSING AND IMAGING  
HARDWARE

| Sensor    | Details   |
|-----------|---|
| Camera    | <b>Type:</b> FLIR BFS-U3-31S4C-C<br>RGB channels, $2048 \times 1536$ resolution,<br>55Hz max frame rate (20Hz in experiment),<br>global shutter |
| Lens      | <b>Type:</b> Chiopt FA0401C<br>82.9° horizontal FOV, 66.5° vertical FOV,<br>4~75 mm focal length  |
| GNSS      | <b>Type:</b> NovAtel OEM718D<br>Dual-antenna, 5 Hz update,<br>1.5 m (RMS) with single point,<br>1cm + 1ppm (RMS) with RTK                       |
| Altimeter | <b>Type:</b> Benewake TF350<br>10Hz update, 350m maximum<br>detection range with 0.1m accuracy  |

and symmetrically crop the associated physical area from the satellite maps to simulate altitude variations. Specifically, we acquired up-to-date satellite maps over regions of approximately  $45 \text{ km}^2$  in the outskirts of Beijing and the urban area of Shanghai, respectively. The altitude range was set to 100–700 m, and for each region, 500 UTM–altitude pairs were sampled randomly. The satellite maps were then cropped according to the nominal camera intrinsics used for synthesis. To better approximate UAV-acquired imagery and evaluate robustness to image-quality degradation, each synthesized image was further perturbed by zero-mean Gaussian noise with standard deviation  $\sigma = 2$  and JPEG compression with quality factor  $q = 95$ , which mimic sensor noise and transmission/storage artifacts, respectively [29].

The VPR network is trained using historical satellite maps from the respective regions, with the search areas for CT01 and CT02 covering  $7.8 \times 5.9 \text{ km}$  and  $8.8 \times 4.9 \text{ km}$ , respectively. The synthetic query images are generated from up-to-date satellite maps, whereas the VPR training and reference database are constructed from historical satellite maps, so that query and reference imagery are temporally separated. For the self-collected datasets, the detailed specifications and parameters of the data acquisition sensors mounted on the UAV platform are presented in Table II. The onboard camera captures images at a resolution of  $2048 \times 1536$  pixels, with a focal length of  $f = 1200$  pixels. The flight datasets (QD01 and QD02) were collected in the Jimo and Chengyang Districts of Qingdao. For QD01 and QD02, the relative-altitude ground truth was obtained by subtracting the local DEM elevation from the barometer-based altitude estimate at each image location. In these datasets, the ground predominantly consists of farmland, which increases perceptual aliasing relative to structured urban scenes. The numbers of test images in QD01 and QD02 are 814 and 470, respectively. The flight altitude range spans 100–650 m. The search areas for QD01 and QD02 are identical, each covering  $4.8 \times 3.5 \text{ km}$ . Detailed information on the test datasets is provided in Table III. Together, these four datasets provide complementary evaluation settings spanning synthetic cross-altitude simulation and real-flight rural testing under substantial scale variation.

## B. Experimental Setup

1) *Hyperparameter choices:* We set the altitude interval  $\Delta H = 50 \text{ m}$  in the main experiments to balance estimation precision and class granularity. Smaller intervals substantially increase the number of classes while reducing the number of samples per class, which makes training less stable and increases overfitting risk. Conversely, larger intervals reduce altitude resolution and introduce additional scale mismatch during cropping. The choice  $\Delta H = 50 \text{ m}$  provides a good compromise between estimation accuracy and class stability, as supported by the comparative results in Table VIII. A detailed analysis of this trade-off and the adaptive binning strategy is provided in Section IV-E3.

For place classification, we set the grid size to  $M = 100 \text{ m}$ , consistent with the reference-database construction process. Reference tiles are cropped sequentially with a stride of approximately one third to one quarter of the tile edge, corresponding to a ground-footprint shift of 60–70 m. This stride defines the effective spatial resolution of the database, implying that tile-level retrieval cannot localize a query more precisely than the tile spacing itself. Therefore,  $M = 100 \text{ m}$  is a natural setting for coarse localization or geo-initialization. Any finer localization would require additional local matching or geometric refinement stages beyond the current pipeline. For group-wise place classification, we set the grouping parameter to  $N = 2$ , which partitions the spatial domain into four groups. This choice follows the empirical design of Divide & Classify (D&C), where  $N = 2$  was reported to provide the best trade-off between learnability and spatial separation among neighboring classes in the city-scale setting [6]. In our setting, using  $N = 2$  reduces the number of classes handled by each classifier and alleviates boundary ambiguity between adjacent grid regions, while keeping the grouping structure simple enough for stable training.

2) *Implementation details:* In the altitude estimation module, the altitude classes are defined according to Eq. (8) with  $\Delta H = 50 \text{ m}$ . For example, choosing  $H_{\min} = 100 \text{ m}$ ,  $H_{\max} = 700 \text{ m}$ , and  $\Delta H = 50 \text{ m}$  yields  $n = (H_{\max} - H_{\min})/\Delta H = 12$  altitude classes. The corresponding class-center altitudes are  $\mathcal{H}_{\text{center}} = \{125, 175, \dots, 675\} \text{ m}$ . During offline data preparation, training samples are generated with a finer altitude sampling interval of  $\delta H = 5 \text{ m}$  (i.e.,  $\{100, 105, 110, \dots, 695\} \text{ m}$ ) and are then assigned to their respective target classes. Unless otherwise specified, both the altitude estimation module and the VPR module use the same optimizer, scheduler, batch size, and stopping criterion.

For training, we use the Adam optimizer together with the ReduceLRonPlateau scheduler. The batch size is set to 64. The initial learning rate for the feature extractor is set to  $1 \times 10^{-4}$ , while the classifier learning rate is set to  $1 \times 10^{-2}$ . The scheduler patience is set to 10 epochs. Training is terminated when the learning rate of the first optimizer parameter group falls below  $1 \times 10^{-6}$ . The classifier parameters are configured as  $m = 0.2$  and  $s = 100$ . In the Spat2Freq module, the nonlinear mapping parameter is set to  $b = 1.5$ . For altitude estimation, the input image size is  $336 \times 448$ . We adopt a cropped ResNet50 backbone, truncate the fourth

TABLE III  
SUMMARY OF THE FOUR EVALUATION DATASETS

| Datasets | Region   | Acquisition Method                     | Number of Test Images | Size of Search Area | Altitude Range |
|----------|----------|--|-----------------------|---------------------|----------------|
| CT01     | Beijing  | Cropped satellite map with degradation | 500                   | $7.8 \times 5.9$ km | 100–700 m      |
| CT02     | Shanghai | Cropped satellite map with degradation | 500                   | $8.8 \times 4.9$ km | 100–650 m      |
| QD01     | Qingdao  | UAV real-flight                        | 814                   | $4.8 \times 3.5$ km | 100m–650m      |
| QD02     | Qingdao  | UAV real-flight                        | 470                   | $4.8 \times 3.5$ km | 100m–650m      |

residual stage, and use MixVPR as the feature aggregator. The backbone is initialized from the default ImageNet-pretrained weights provided by PyTorch. During training, color jittering is applied to improve robustness to illumination variation.

In the VPR module, we set the grid cell size to  $M = 100$  m and the grouping parameter to  $N = 2$ , which partitions the spatial domain into four groups ( $|G| = 4$ ). The classifier configuration and learning-rate settings are the same as those used in the altitude classification module. The input image size is  $224 \times 224$ . During training, the ground-plane footprint of each image is computed using Eq. (13), and the canonical altitude is set to  $H_{db} = 125$  m. This value corresponds to the center of the first altitude interval [100, 150) m under the main fixed-interval setting and is therefore used as the canonical reference scale for query normalization and database construction. The feature extraction backbone is EfficientNet-B5, combined with MixVPR for aggregation, and it is initialized from the default ImageNet-pretrained weights provided by PyTorch.

3) *Metrics*: For altitude estimation, we consider the mean altitude estimation error  $E_{avg}$  and the percentage of estimates with error below a threshold  $D$ , denoted as  $P_{E < D}$ . In VPR evaluation, we measure performance using the standard retrieval recall at rank  $N$  (R@N), which quantifies the proportion of queries for which at least one correctly matched reference image appears among the top- $N$  retrieved candidates. Specifically, we use R@1 and R@5 as evaluation criteria. Once the initial localization coordinates are obtained, we compute the localization error for each query as the Euclidean distance between the estimated UTM coordinates and the ground-truth UTM coordinates, and report the corresponding mean value as  $d_{avg}$ . A query is considered successfully localized when its Euclidean UTM error is below 100 m. This threshold is not chosen merely to match the 100 m classification grid size; rather, it is intended to evaluate the system as a coarse-localization or geo-initialization module and is consistent with the effective database spatial resolution induced by the 60–70 m reference-tile stride discussed above.

4) *Baselines and References*: To ensure fair comparisons, all trainable VPR variants are evaluated under aligned training protocols, including matched batch sizes, data augmentation strategies, and dataset splits.

a) *Altitude Estimation References*: In UAV applications, relative altitude ground truth is typically obtained via non-visual sources such as barometric measurements, laser/range-based altimeters, or DEM alignment. These signals are used in our datasets to generate altitude annotations, but they rely on external data or hardware and therefore cannot serve as baselines for evaluating vision-only approaches.

To the best of our knowledge, no closely matched vision-only baseline is available for our exact setting: single-image global relative-altitude estimation from nadir-view aerial imagery without target-domain real flight data for training. Therefore, we include monocular metric depth estimation (MMDE) models as contextual references. Among existing vision-based techniques, MMDE models such as Depth Anything V2 and UniDepth V2 are the closest contextual references to our task, as they infer geometric quantities from a single image. However, they are designed for dense pixel-wise depth prediction rather than global altitude estimation. For reference, we apply Depth Anything V2 [15] and UniDepth V2 [16], and compute the arithmetic mean of the predicted depth map as the estimated relative altitude  $\hat{H}$ . These results are reported only for contextual comparison rather than as formal baselines, and help clarify the differences in task formulation between dense depth prediction and the present relative-altitude-estimation problem.

b) *VPR Baselines*: For VPR comparison, we evaluate MixVPR [2], CosPlace [5], CricaVPR [30], and DINOv2-SALAD [31] as baseline models. MixVPR and CosPlace use CNN-based feature extractors, whereas CricaVPR and DINOv2-SALAD adopt DINOv2-based [32] ViT feature extractors.

### C. Main Results

We first report the VPR results to evaluate the plug-and-play effect of the proposed relative altitude estimation module across different VPR pipelines. The results are summarized in Table IV. Incorporating relative altitude estimation yields clear overall improvements across diverse VPR architectures. When averaged over the four datasets, R@1 improves by 40.84, 27.47, 20.95, 21.95, and 41.50 percentage points for MixVPR, CosPlace, SALAD, CricaVPR, and our VPR module, respectively. The corresponding average R@5 improvements are 57.08, 40.62, 40.56, 39.50, and 56.83 percentage points. These results show that compensating for scale discrepancies via relative altitude estimation substantially improves retrieval robustness under varying flight altitudes. Notably, although the DINOv2-based methods (SALAD and CricaVPR) already exhibit stronger cross-altitude robustness without RAE, they still benefit overall from the proposed altitude normalization, especially in terms of average performance and higher-rank recall.

### D. Real-Time Performance

To evaluate the computational efficiency of the proposed framework, we conducted runtime analysis on a workstation

TABLE IV

RESULTS OF DIFFERENT VPR METHODS WITH AND WITHOUT RELATIVE ALTITUDE ESTIMATION (RAE). BOLD AND UNDERLINED VALUES DENOTE THE BEST AND SECOND-BEST RESULTS IN EACH COLUMN, RESPECTIVELY. ✓ AND ✗ INDICATE WITH AND WITHOUT RAE.

| Method         | RAE | CT01         |              | CT02         |              | QD01         |              | QD02         |              |
|----------------|-----|--------------|--------------|--------------|--------------|--------------|--------------|--------------|--------------|
|                |     | R@1↑         | R@5↑         | R@1↑         | R@5↑         | R@1↑         | R@5↑         | R@1↑         | R@5↑         |
| MixVPR         | ✓   | 63.80        | 87.80        | 62.20        | 80.00        | 32.80        | 60.69        | <u>46.81</u> | 57.87        |
|                | ✗   | 16.40        | 16.80        | 15.40        | 16.60        | 7.25         | 20.39        | 3.19         | 4.26         |
| CosPlace       | ✓   | 50.40        | 67.00        | 44.80        | 59.00        | 32.80        | 46.93        | 30.00        | 44.26        |
|                | ✗   | 14.20        | 15.00        | 16.00        | 16.80        | 16.22        | 18.67        | 1.70         | 4.26         |
| SALAD          | ✓   | 60.70        | <u>95.20</u> | <u>64.40</u> | <u>88.60</u> | <u>53.62</u> | <u>75.80</u> | 45.32        | <u>66.53</u> |
|                | ✗   | 29.80        | 32.60        | 26.80        | 31.00        | 43.00        | 49.02        | 40.64        | 51.28        |
| CricaVPR       | ✓   | <u>66.40</u> | 87.60        | 56.80        | 75.60        | 53.07        | <u>75.80</u> | 36.17        | 61.49        |
|                | ✗   | 21.80        | 22.80        | 18.20        | 19.20        | 46.56        | 52.21        | 38.09        | 48.30        |
| Our VPR Module | ✓   | <b>77.20</b> | <b>97.20</b> | <b>68.40</b> | <b>90.80</b> | <b>54.67</b> | <b>78.01</b> | <b>47.45</b> | <b>67.23</b> |
|                | ✗   | 26.80        | 29.20        | 24.60        | 26.80        | 19.04        | 24.82        | 11.28        | 25.11        |

equipped with a single NVIDIA GeForce RTX 4090 GPU and an AMD EPYC 7352 CPU with 11 vCPUs. Table V summarizes the average and maximum latency, peak CPU/GPU memory usage, and overall throughput in frames per second (FPS) for each module in the current implementation: relative altitude estimation (RAE), altitude-aware cropping (Crop), VPR classification (VPR (C)), and VPR retrieval (VPR (R)). Here, Peak CPU ABS denotes the absolute peak CPU memory observed during each module, whereas CPU DELTA denotes the incremental CPU memory increase relative to the module entry point.

The results show that RAE and cropping are lightweight, with average latencies of 10.7 ms and 12.4 ms, respectively. The classification stage is the most computationally demanding, averaging 50.6 ms per query, while retrieval over candidate classes adds only 1.5 ms. Peak GPU memory usage remains below 600 MB for all modules, and CPU memory consumption is modest, with incremental usage under 100 MB per stage. The full pipeline reaches 13.3 FPS on the reported workstation hardware, indicating compatibility with online processing at 10–15 Hz in the present implementation. These results indicate that the proposed pipeline is computationally efficient in the current implementation and compatible with online processing, although dedicated onboard benchmarking is still needed for deployment on airborne platforms.

TABLE V  
RUNTIME STATISTICS OF THE PROPOSED PIPELINE

| Metric            | RAE    | Crop   | VPR (C) | VPR (R) |
|-------------------|--------|--------|---------|---------|
| Avg latency (ms)  | 10.7   | 12.4   | 50.6    | 1.5     |
| Max latency (ms)  | 14.0   | 36.5   | 92.7    | 4.0     |
| Peak CPU ABS (MB) | 260.57 | 679.81 | 1830.71 | 1830.74 |
| CPU DELTA (MB)    | 0.48   | 21.09  | 70.45   | 2.74    |
| Peak GPU (MB)     | 54.77  | 0.00   | 574.67  | 429.36  |
| Overall FPS       | 13.3   |        |         |         |

### E. Ablation Study

1) *Image Pre-processing*: To evaluate the usefulness of the proposed Spat2Freq image pre-processing module for the relative altitude estimation task, we compare models trained

on Spat2Freq-processed images with models trained directly on spatial-domain images. Table VI summarizes the average altitude estimation error and threshold-based estimation accuracy under two configurations: with and without Spat2Freq. Figure 6 provides a visual comparison of the estimated relative altitudes across the four datasets (CT01, CT02, QD01, and QD02), illustrating the difference between the two settings. In each subfigure, every point represents a single query image, with the ground-truth relative altitude on the horizontal axis and the estimated relative altitude on the vertical axis. Green points correspond to models trained without Spat2Freq, while blue points correspond to models trained with Spat2Freq. The yellow diagonal line indicates perfect estimation, i.e., cases where  $\hat{H}$  equals the ground-truth relative altitude. Three pairs of symmetrically placed dashed lines represent error thresholds of  $\pm 25$  m (purple),  $\pm 50$  m (red), and  $\pm 100$  m (dark blue), respectively. As shown in Fig. 6, the model trained with Spat2Freq produces estimates that are more concentrated around the diagonal and more frequently fall within the predefined error bands, indicating improved altitude estimation accuracy.

2) *Classifier*: We next compare three classifier formulations under otherwise identical settings: (1) a standard fully connected classifier trained with cross-entropy loss (CE), (2) the additive angular margin classifier (AAMC) trained with ArcFace loss, and (3) the proposed quality-adaptive margin classifier (QAMC), whose margin formulation is adapted from AdaFace. We integrate these classifiers into the same VPR pipeline while keeping the remaining components unchanged, and then evaluate the impact of the classifier formulation on retrieval performance. The results are summarized in Table VII. Overall, QAMC yields the strongest average retrieval performance across the evaluated datasets and recall levels, although the best result for an individual dataset/metric is not always achieved by QAMC.

3) *Altitude Interval Size*: We further analyze the impact of altitude interval size  $\Delta H$  on relative altitude estimation and downstream VPR performance. As shown in Table VIII, fixed intervals exhibit a clear trade-off: smaller bins (e.g., 25 m) improve fine-grained accuracy at tight thresholds ( $P_{E<25}$ ,  $P_{E<50}$ ) but suffer from enlarged class sets and reduced per-

TABLE VI  
RELATIVE ALTITUDE ESTIMATION WITH AND WITHOUT Spat2Freq

| Spat2Freq | CT01         |              |              |               | CT02         |              |              |               |
|-----------|--------------|--------------|--------------|---------------|--------------|--------------|--------------|---------------|
|           | $E_{avg}$ ↓  | $P_{E<25}$ ↑ | $P_{E<50}$ ↑ | $P_{E<100}$ ↑ | $E_{avg}$ ↓  | $P_{E<25}$ ↑ | $P_{E<50}$ ↑ | $P_{E<100}$ ↑ |
| ✓         | <b>17.75</b> | <b>79.80</b> | <b>97.80</b> | <b>99.60</b>  | <b>21.10</b> | <b>74.40</b> | <b>95.40</b> | <b>99.00</b>  |
| ✗         | 29.33        | 62.00        | 83.60        | 95.60         | 25.99        | 60.40        | 85.20        | 98.80         |

| Spat2Freq | QD01         |              |              |               | QD02         |              |              |               |
|-----------|--------------|--------------|--------------|---------------|--------------|--------------|--------------|---------------|
|           | $E_{avg}$ ↓  | $P_{E<25}$ ↑ | $P_{E<50}$ ↑ | $P_{E<100}$ ↑ | $E_{avg}$ ↓  | $P_{E<25}$ ↑ | $P_{E<50}$ ↑ | $P_{E<100}$ ↑ |
| ✓         | <b>59.42</b> | <b>43.00</b> | <b>67.74</b> | <b>78.75</b>  | <b>47.96</b> | <b>47.45</b> | <b>74.04</b> | <b>84.68</b>  |
| ✗         | 73.35        | 39.80        | 56.63        | 75.43         | 60.97        | 31.91        | 60.00        | 82.34         |

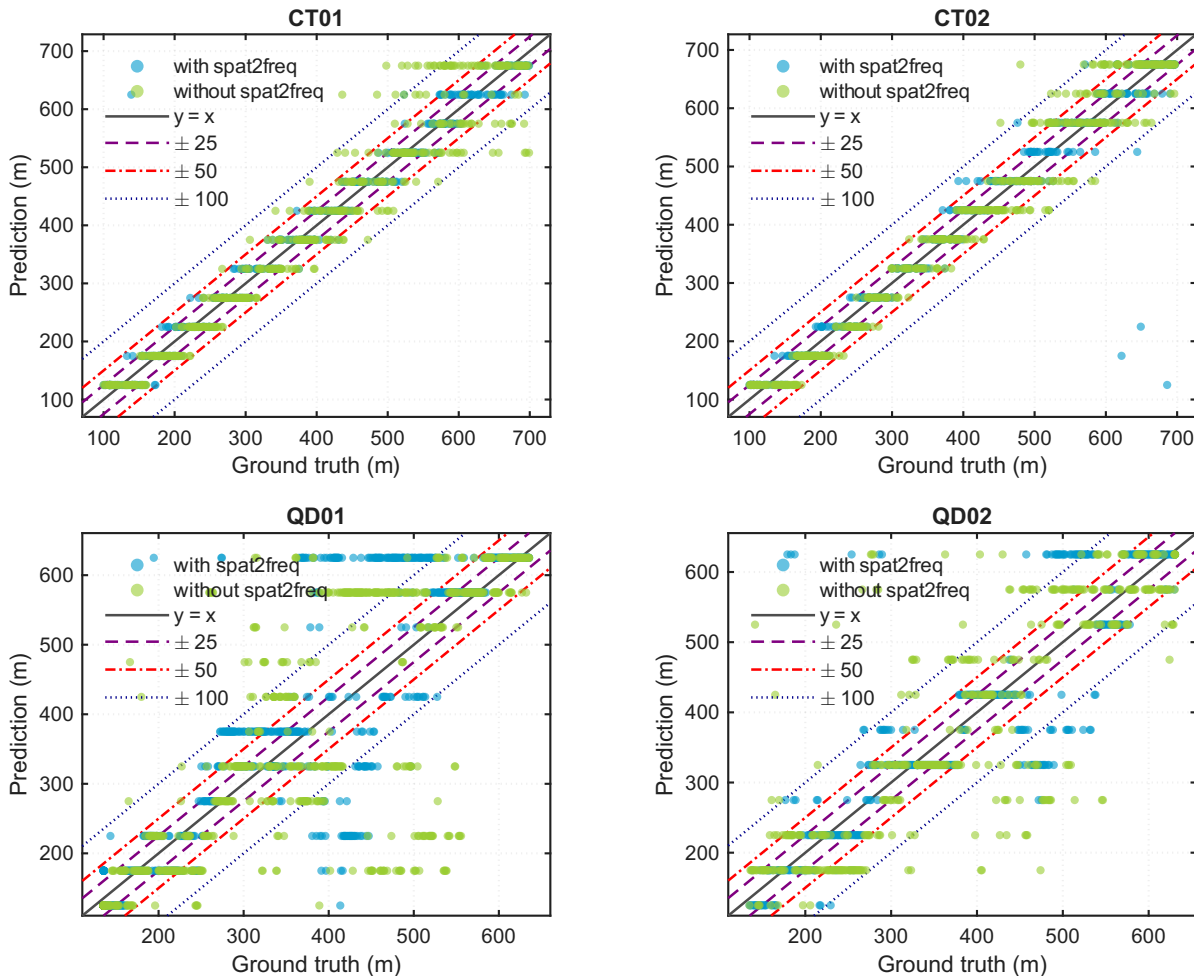


Fig. 6. Scatter plots of relative altitude estimation results with and without Spat2Freq. Green and blue points denote models trained without and with Spat2Freq, respectively. The diagonal line indicates perfect estimation, and the dashed bands correspond to  $\pm 25$ ,  $\pm 50$ , and  $\pm 100$  m errors.

TABLE VII  
RESULTS WITH DIFFERENT CLASSIFIER FORMULATIONS. BOLD VALUES DENOTE THE BEST RESULT IN EACH COLUMN.

| Method | CT01         |              | CT02         |              | QD01         |              | QD02         |              |
|--------|--------------|--------------|--------------|--------------|--------------|--------------|--------------|--------------|
|        | R@1↑         | R@5↑         | R@1↑         | R@5↑         | R@1↑         | R@5↑         | R@1↑         | R@5↑         |
| QAMC   | <b>77.60</b> | <b>98.20</b> | 71.20        | <b>93.60</b> | <b>55.46</b> | <b>81.08</b> | 51.55        | <b>74.89</b> |
| AAMC   | 72.00        | 93.20        | <b>73.00</b> | 93.00        | 51.74        | 74.45        | 50.55        | 68.09        |
| CE     | 68.80        | 92.60        | 63.80        | 84.20        | 50.61        | 75.92        | <b>52.13</b> | 71.28        |

class samples, leading to unstable retrieval. Conversely, coarse bins (e.g., 100 m) simplify training but degrade estimation

accuracy ( $E_{avg}$ ) and retrieval performance due to mismatched cropping ratios. Intermediate settings (50–75 m) achieve more

balanced results, with  $\Delta H = 50$  often yielding the best compromise between estimation error and retrieval recall.

To better account for the nonlinear relation between altitude and cropping ratio, we further design a variable-interval strategy based on an exponential function. Specifically, we set  $H_0 = 100$  m as the starting altitude,  $\Delta_0 = 20$  m as the base interval, and  $r = 1.1$  as the growth rate. The lower bound of the  $k$ -th interval is defined by the cumulative geometric progression

$$H_k = H_0 + \Delta_0 \cdot \frac{r^k - 1}{r - 1}, \quad k \in \mathbb{Z}_{\geq 0},$$

and the corresponding interval is

$$I_k = \{H \mid H_k \leq H < H_{k+1}\}.$$

Given an input altitude  $H \in [H_0, H_{\max})$ , the corresponding interval index  $k^*$  under the exponential binning rule is

$$k^* = \left\lceil \log_r \left( 1 + \frac{(H - H_0)(r - 1)}{\Delta_0} \right) \right\rceil,$$

which assigns  $H$  to its interval via the inverse of the cumulative spacing. The center altitude of the  $k$ -th interval is defined as

$$H_{\text{center,var}}^{(k)} = \frac{H_k + H_{k+1}}{2} = H_0 + \Delta_0 \cdot \frac{r^k - 1}{r - 1} + \frac{1}{2} \Delta_0 r^k.$$

Accordingly, the set of center altitudes associated with the variable-interval scheme is

$$\mathcal{H}_{\text{center,var}} = \left\{ H_{\text{center,var}}^{(k)} \mid k \in \mathbb{Z}_{\geq 0} \right\}.$$

The corresponding class-to-altitude mapping is then defined as

$$\text{Class2Alt}_{\text{var}}(k) = H_{\text{center,var}}^{(k)}, \quad k \in \mathbb{Z}_{\geq 0}.$$

Accordingly, the estimated altitude under the variable-interval scheme is obtained as  $\hat{H} = \text{Class2Alt}_{\text{var}}(k^*)$ . Together, these expressions are intended to make each altitude bin correspond to a more uniform change in cropping ratio: finer bins are allocated at lower altitudes, where the same absolute altitude change induces a larger relative change in image scale, while coarser bins are allocated at higher altitudes, where the relative change in image scale becomes smaller.

The results in Table VIII show that adaptive binning is competitive with fixed-interval schemes and can improve the trade-off between estimation accuracy and downstream retrieval performance in several settings. Across all datasets, the altitude interval size  $\Delta H$  plays a critical role in balancing estimation precision and retrieval robustness. Fixed intervals offer predictable behavior but suffer from either over-fragmentation (e.g., small  $\Delta H$  leading to sparse class samples) or excessive coarseness (e.g., large  $\Delta H$  causing scale mismatch). In contrast, the exponential binning strategy can improve performance in several cases by matching bin granularity to scale sensitivity, thereby reducing low-altitude ambiguity and mitigating excessive coarseness at higher altitudes. Nevertheless, since the variable-interval scheme does not dominate every dataset and metric, we retain the fixed  $\Delta H = 50$  m setting in the main experiments because it offers a simpler and more interpretable experimental configuration while still achieving competitive overall performance.

4) *Relative Altitude Estimation*: To further contextualize the performance of the proposed relative altitude estimation module, we compare it with two recent representative monocular metric depth estimation (MMDE) models, namely Depth Anything V2 and UniDepth V2. The results are shown in Table IX.

Since MMDE algorithms output dense depth maps, we use the arithmetic mean of each predicted depth map as a coarse scalar reference and feed it into the same downstream crop-and-retrieval pipeline. As shown in Table IX, these task-mismatched zero-shot references do not provide reliable global relative-altitude priors in our setting. We therefore report them only to illustrate the gap between dense monocular depth prediction and the present relative-altitude-estimation task, rather than as formal competing baselines. All downstream R@1 and R@5 values in Table IX are obtained by feeding each scalar altitude reference into the same crop-and-retrieval pipeline. Although UniDepth V2 attains a comparable R@5 on QD02, its altitude estimates remain substantially less accurate overall than those of the proposed task-specific module.

5) *Localization Refinement with Weighted Coordinate Estimation (WCE) and Outlier Filtering*: We propose a method to estimate the UTM coordinate  $\text{UTM}^* = (\text{UTM}_e^*, \text{UTM}_n^*)$  and refine the localization result of a query image based on the retrieved candidates from VPR, incorporating a one-class support vector machine (SVM)-based [33] outlier filtering strategy. Let  $d_q \in \mathbb{R}^d$  denote the global feature vector of the query image. From the retrieval process, the top  $n_{\text{retrieve}}$  reference images are obtained, each associated with a global feature vector and a corresponding UTM coordinate. Denote the set of retrieved global features by

$$\mathcal{V} = \{d_i \in \mathbb{R}^d \mid i = 1, 2, \dots, n_{\text{retrieve}}\},$$

and the corresponding UTM coordinate set by

$$\mathcal{U} = \{\text{UTM}_i = (\text{UTM}_{e,i}, \text{UTM}_{n,i}) \mid i = 1, 2, \dots, n_{\text{retrieve}}\}.$$

To filter unreliable localization candidates, we fit a one-class SVM [34] to the retrieved coordinate set  $\mathcal{U}$  for each query, using kernel  $K$ . The resulting decision function is

$$f_{\text{oc}}(u) = w \cdot \phi(u) - \rho,$$

where  $\phi(u)$  denotes the kernel feature map,  $w$  is the learned hyperplane weight, and  $\rho$  is the decision offset. The filtered UTM coordinate set is then defined by

$$\mathcal{U}_{\text{filtered}} = \{\text{UTM}_i \in \mathcal{U} \mid f_{\text{oc}}(\text{UTM}_i) \geq 0\},$$

with inliers retained and outliers discarded. For brevity, this filtering is denoted as

$$\mathcal{U}_{\text{filtered}} = \text{SVM}_{\text{oc}}(\mathcal{U}).$$

We further define the retained index set as

$$\mathcal{I}_{\text{filtered}} = \{i \in \{1, \dots, n_{\text{retrieve}}\} \mid \text{UTM}_i \in \mathcal{U}_{\text{filtered}}\}.$$

To compute the final localization estimate, each retained feature vector is assigned a weight inversely proportional to its Euclidean distance from the query vector:

$$w_i = \frac{1}{\|d_q - d_i\|_2 + \epsilon}, \quad i \in \mathcal{I}_{\text{filtered}},$$

TABLE VIII

COMPARISON OF DIFFERENT ALTITUDE-INTERVAL SETTINGS. ‘‘VARIABLE’’ DENOTES THE PROPOSED EXPONENTIAL VARIABLE-INTERVAL SCHEME. BOLD AND UNDERLINED VALUES DENOTE THE BEST AND SECOND-BEST RESULTS IN EACH COLUMN, RESPECTIVELY.

| $\Delta H$ | CT01         |              |              |               |              |              | CT02         |              |              |               |              |              |
|------------|--------------|--------------|--------------|---------------|--------------|--------------|--------------|--------------|--------------|---------------|--------------|--------------|
|            | $E_{avg}$    | $P_{E<25}$   | $P_{E<50}$   | $P_{E<100}$   | R@1          | R@5          | $E_{avg}$    | $P_{E<25}$   | $P_{E<50}$   | $P_{E<100}$   | R@1          | R@5          |
| 25         | 20.35        | 69.40        | 91.40        | 99.60         | 77.60        | <b>98.20</b> | 22.50        | 65.40        | 89.80        | <b>100.00</b> | 61.40        | 92.60        |
| 50         | <b>17.75</b> | <b>79.80</b> | <b>97.80</b> | <b>100.00</b> | 77.20        | 97.20        | <u>21.10</u> | <b>74.40</b> | <b>95.40</b> | 99.00         | <b>68.40</b> | 90.80        |
| 75         | 24.69        | 54.80        | 92.00        | <u>99.80</u>  | <b>79.00</b> | <u>97.80</u> | 24.98        | 58.00        | 90.20        | 99.20         | <u>68.00</u> | 86.80        |
| 100        | 27.81        | 47.60        | 88.60        | <u>99.80</u>  | 64.00        | 90.20        | 29.19        | 45.20        | 85.40        | <u>99.60</u>  | 56.80        | 80.60        |
| Variable   | <u>18.90</u> | <u>73.00</u> | <u>94.00</u> | <b>100.00</b> | <u>78.40</u> | <b>98.20</b> | <b>18.95</b> | <u>69.80</u> | <u>93.40</u> | <b>100.00</b> | <b>68.40</b> | <b>93.60</b> |

| $\Delta H$ | QD01         |              |              |              |              |              | QD02         |              |              |              |              |              |
|------------|--------------|--------------|--------------|--------------|--------------|--------------|--------------|--------------|--------------|--------------|--------------|--------------|
|            | $E_{avg}$    | $P_{E<25}$   | $P_{E<50}$   | $P_{E<100}$  | R@1          | R@5          | $E_{avg}$    | $P_{E<25}$   | $P_{E<50}$   | $P_{E<100}$  | R@1          | R@5          |
| 25         | <b>47.06</b> | <u>38.33</u> | <u>59.09</u> | <b>86.49</b> | 52.95        | 72.97        | 52.47        | 25.53        | 52.98        | <u>90.43</u> | <u>51.06</u> | 65.96        |
| 50         | 59.42        | <b>43.00</b> | <b>64.74</b> | 78.75        | <u>54.67</u> | <b>78.01</b> | <u>47.96</u> | <b>47.45</b> | <b>74.04</b> | 84.68        | 47.45        | <u>67.23</u> |
| 75         | 58.57        | 28.01        | 47.42        | <u>83.29</u> | 43.98        | 59.58        | 61.43        | 28.94        | 56.60        | 86.17        | 40.43        | 67.02        |
| 100        | 93.92        | 36.86        | 56.02        | 71.01        | 48.28        | 61.06        | 58.35        | <u>34.89</u> | <u>62.55</u> | 84.89        | 42.13        | <b>71.06</b> |
| Variable   | <u>57.31</u> | 34.40        | 53.32        | 78.99        | <b>56.76</b> | <u>74.08</u> | <b>46.18</b> | 32.98        | 57.66        | <b>92.34</b> | <b>51.49</b> | 65.96        |

TABLE IX

COMPARISON WITH MMDE CONTEXT REFERENCES UNDER THE SAME DOWNSTREAM CROP-AND-RETRIEVAL PIPELINE

| Method            | CT01         |              |              |               |              |              | CT02         |              |              |              |              |              |
|-------------------|--------------|--------------|--------------|---------------|--------------|--------------|--------------|--------------|--------------|--------------|--------------|--------------|
|                   | $E_{avg}$    | $P_{E<25}$   | $P_{E<50}$   | $P_{E<100}$   | R@1          | R@5          | $E_{avg}$    | $P_{E<25}$   | $P_{E<50}$   | $P_{E<100}$  | R@1          | R@5          |
| UniDepth V2       | 271.61       | 0.80         | 2.00         | 13.60         | 30.20        | 32.40        | 288.64       | 1.00         | 2.00         | 13.80        | 25.40        | 27.80        |
| Depth Anything V2 | 281.70       | 6.20         | 11.00        | 18.80         | 26.80        | 29.20        | 299.25       | 6.40         | 9.40         | 21.00        | 24.80        | 27.00        |
| Ours              | <b>17.75</b> | <b>79.80</b> | <b>97.80</b> | <b>100.00</b> | <b>77.20</b> | <b>97.20</b> | <b>21.10</b> | <b>74.40</b> | <b>95.40</b> | <b>99.00</b> | <b>68.40</b> | <b>90.80</b> |

| Method            | QD01         |              |              |              |              |              | QD02         |              |              |              |              |              |
|-------------------|--------------|--------------|--------------|--------------|--------------|--------------|--------------|--------------|--------------|--------------|--------------|--------------|
|                   | $E_{avg}$    | $P_{E<25}$   | $P_{E<50}$   | $P_{E<100}$  | R@1          | R@5          | $E_{avg}$    | $P_{E<25}$   | $P_{E<50}$   | $P_{E<100}$  | R@1          | R@5          |
| UniDepth V2       | 174.91       | 0.00         | 1.23         | 26.90        | 39.68        | 59.83        | 179.10       | 0.00         | 1.49         | 13.83        | 47.23        | <b>67.87</b> |
| Depth Anything V2 | 239.92       | 1.23         | 20.02        | 28.38        | 19.04        | 25.31        | 264.17       | 3.83         | 10.85        | 18.09        | 13.19        | 27.66        |
| Ours              | <b>59.42</b> | <b>43.00</b> | <b>64.74</b> | <b>78.75</b> | <b>54.67</b> | <b>78.01</b> | <b>47.96</b> | <b>47.45</b> | <b>74.04</b> | <b>84.68</b> | <b>47.45</b> | 67.23        |

- MMDE models are not designed for altitude estimation; they are included as context references only.

where  $\epsilon$  is a small positive constant to prevent division by zero. These weights are then normalized over the retained set:

$$\tilde{w}_i = \frac{w_i}{\sum_{j \in \mathcal{I}_{\text{filtered}}} w_j}, \quad i \in \mathcal{I}_{\text{filtered}}.$$

The estimated UTM coordinate is computed as a weighted average over the retained candidates:

$$\text{UTM}^* = \sum_{i \in \mathcal{I}_{\text{filtered}}} \tilde{w}_i \text{UTM}_i,$$

where  $\text{UTM}^*$  denotes the final predicted location.

We refer to this process as weighted coordinate estimation (WCE), which computes  $\text{UTM}^*$  from the retrieved global feature set  $\mathcal{V}$ , the corresponding coordinate set  $\mathcal{U}$ , and the query feature  $d_q$ , formally expressed as

$$\text{UTM}^* = \text{WCE}(d_q, \mathcal{V}, \mathcal{U}).$$

For comparison, the baseline without WCE directly takes the UTM coordinate of the top-1 retrieved candidate as the final localization estimate.

Table X compares the localization success rate between the top-1 baseline and the WCE-enhanced approach. The reported metric is the localization success rate,  $S_{\text{Loc}}$ , which is defined as

TABLE X  
LOCALIZATION SUCCESS RATE  $S_{\text{Loc}}$  WITH AND WITHOUT WEIGHTED COORDINATE ESTIMATION (WCE)

| WCE | CT01         | CT02         | QD01         | QD02         |
|-----|--------------|--------------|--------------|--------------|
| ✓   | <b>96.20</b> | <b>87.00</b> | <b>69.78</b> | <b>59.57</b> |
| ✗   | 77.20        | 68.40        | 54.67        | 47.45        |

the proportion of test images whose estimated UTM coordinate lies within 100 meters of the ground-truth location. Formally,

$$S_{\text{Loc}} = \frac{N_{\text{success}}}{N_{\text{total}}} \times 100\%,$$

where  $N_{\text{success}}$  denotes the number of successful queries, and  $N_{\text{total}}$  is the total number of evaluated queries. Table X shows that, across all datasets,  $S_{\text{Loc}}$  is consistently higher with WCE than without it. This indicates that aggregating multiple retrieved candidates with feature-distance-based weighting and one-class SVM outlier filtering can improve robustness to noisy matches and yield more reliable coarse localization.

## V. DISCUSSION

### A. Scalability and Grid Partitioning Strategy

The proposed VPR module adopts a grid-based classification with a fixed cell size (e.g., 100 m). We emphasize that the

spatial partition must be defined as a hyperparameter prior to training and inference, rather than being adaptively adjusted at runtime. This constraint arises because class labels are tied to specific spatial cells: if the boundaries were dynamically altered, the correspondence between training and inference labels would be broken, rendering the classifier inconsistent. Therefore, fixed discretization is a necessary condition to ensure reproducibility and stable training.

The cell size of 100 m is selected to match the resolution of the database construction process. Specifically, reference tiles are cropped sequentially with a stride of approximately one third to one quarter of the tile edge, corresponding to a ground footprint shift of 60 to 70 m. Consequently, 100 m provides a physical resolution for coarse localization initialization. Utilizing smaller cells would result in an excessive number of classes with insufficient training samples per class, whereas larger cells would diminish the estimation accuracy and exacerbate scale mismatches.

Prior works have similarly relied on predefined spatial partitions, albeit employing different strategies. For instance, PlaNet [3] utilizes the S2 geometry library to partition the Earth into hierarchical cells, subsequently merging or splitting these cells based on the geographic density of the training images. The resulting adaptive cells are irregular but remain fixed in boundary and distribution once defined, ensuring consistent labels. CPlaNet [4] employs combinatorial partitioning, HGE [35] adopts hierarchical coarse-to-fine grids, and Divide & Classify [6] utilizes fixed UTM grids. These methodologies demonstrate that spatial boundaries must be established in advance, whether uniformly or adaptively, to enable classification-based localization. In the proposed system, the fixed 100 m grid is effective for the evaluated experimental regions. Scalability to larger-scale deployments can be achieved in future iterations by integrating hierarchical classification or multi-scale retrieval pipelines.

Following the Divide & Classify strategy [6], we partition the spatial domain into  $N = 2$  groups. This reduces the number of classes per classifier, alleviates boundary ambiguity, and improves discriminability. Group-wise classification reduces intra-class variance and improves feature separability, especially when the spatial domain exhibits heterogeneous appearance distributions. Such strategies and hyperparameter setting have been shown to enhance performance in prior city-scale VPR studies, such as Divide & Classify [6] and GeoVINS [8].

### B. Limitations and Future Work

While the proposed framework provides an effective solution for altitude-aware visual place recognition (VPR), several limitations remain to be addressed in future research.

A first limitation is that the current formulation assigns a single global relative-altitude prior to the entire image footprint. In mountainous regions or strongly undulating terrain, local ground elevation may vary substantially within a single image, which can reduce the validity of one global cropping ratio and lead to imperfect scale normalization.

Another limitation is that the Spat2Freq module relies heavily on the spatial distribution of frequency-domain com-

ponents to capture scale variations. In rural or agricultural environments where high-frequency structural features (e.g., buildings and road intersections) are scarce, the frequency spectrum becomes less discriminative, occasionally leading to suboptimal relative altitude estimation. To mitigate this limitation in future iterations, incorporating stronger semantic boundary constraints could be explored. In parallel, geometric enhancements inspired by recent vehicular VPR systems may further improve robustness under challenging urban localization conditions [36].

The framework also fundamentally relies on pre-rendered, high-resolution satellite maps for both offline training and online database retrieval. This introduces a heavy data dependency, limiting its immediate applicability in completely unmapped environments or regions where prior satellite imagery cannot be acquired in advance. Future extensions may investigate cross-modal global localization paradigms that leverage publicly available map priors, such as OpenStreetMap, to reduce reliance on dense geo-referenced imagery and pre-rendered pixel-level databases [37].

Finally, the current architecture utilizes a non-end-to-end, two-stage decoupled pipeline. The altitude estimation and VPR modules are trained independently. Consequently, any altitude estimation error linearly propagates into the cropping stage, and joint parameter optimization during deployment is challenging. Future work will investigate differentiable spatial operations (e.g., spatial transformer networks) to replace the hard cropping step, thereby enabling end-to-end joint training and mitigating cascading errors. Concurrently, we plan to develop a unified backbone architecture with task-specific adapters for both altitude classification and place recognition, which will further streamline the inference pipeline and reduce computational overhead for resource-constrained airborne platforms.

## VI. CONCLUSION

In this paper, we introduce an altitude-adaptive visual place recognition (VPR) framework for airborne platforms. We exploit frequency-domain processing to capture scale-dependent density variations in ground textures caused by altitude changes. We reformulate the continuous relative altitude estimation problem as a discrete classification task by dividing flight altitudes into intervals, which yields robust altitude estimations and facilitates seamless integration with the downstream VPR pipeline. Furthermore, we propose an altitude-guided image cropping mechanism that normalizes variable-scale queries to a fixed-scale primitive map, aligning the spatial scale prior to feature extraction. Extensive experiments across synthetic and real-world UAV flight datasets demonstrate that the proposed method effectively mitigates scale mismatch and achieves high localization accuracy using exclusively visual inputs. To the best of our knowledge, we did not identify prior work that jointly studies single-image, vision-only relative-altitude estimation from nadir-view UAV imagery and uses the estimate as an explicit scale prior for altitude-adaptive aerial visual place recognition, while training the altitude estimator without target-domain real flight images.

## REFERENCES

- [1] R. Arandjelović, P. Gronat, A. Torii, T. Pajdla, and J. Sivic, “NetVLAD: CNN architecture for weakly supervised place recognition,” *IEEE Transactions on Pattern Analysis and Machine Intelligence*, vol. 40, no. 6, pp. 1437–1451, 2018.
- [2] A. Ali-Bey, B. Chaib-Draa, and P. Giguère, “MixVPR: Feature mixing for visual place recognition,” in *2023 IEEE/CVF Winter Conference on Applications of Computer Vision (WACV)*, 2023, pp. 2997–3006.
- [3] T. Weyand, I. Kostrikov, and J. Philbin, “PlaNet - photo geolocation with convolutional neural networks,” in *Computer Vision – ECCV 2016*, B. Leibe, J. Matas, N. Sebe, and M. Welling, Eds. Cham: Springer International Publishing, 2016, pp. 37–55.
- [4] P. H. Seo, T. Weyand, J. Sim, and B. Han, “CPlaNet: Enhancing image geolocalization by combinatorial partitioning of maps,” in *Computer Vision – ECCV 2018*, V. Ferrari, M. Hebert, C. Sminchisescu, and Y. Weiss, Eds. Cham: Springer International Publishing, 2018, pp. 544–560.
- [5] G. Berton, C. Masone, and B. Caputo, “Rethinking visual geolocalization for large-scale applications,” in *2022 IEEE/CVF Conference on Computer Vision and Pattern Recognition (CVPR)*, 2022, pp. 4868–4878.
- [6] G. Trivigno, G. Berton, J. Aragon, B. Caputo, and C. Masone, “Divide&Classify: Fine-grained classification for city-wide visual place recognition,” in *2023 IEEE/CVF International Conference on Computer Vision (ICCV)*, 2023, pp. 11 108–11 118.
- [7] G. Berton, G. Trivigno, B. Caputo, and C. Masone, “EigenPlaces: Training viewpoint robust models for visual place recognition,” in *2023 IEEE/CVF International Conference on Computer Vision (ICCV)*, 2023, pp. 11 046–11 056.
- [8] C. Li, M. He, C. Chen, J. Liu, X. Lyu, G. Huang, and Z. Meng, “GeoVINS: Geographic-visual-inertial navigation system for large-scale drift-free aerial state estimation,” *IEEE Transactions on Robotics*, vol. 41, pp. 5835–5853, 2025.
- [9] A. Cherian, J. Andersh, V. Morellas, N. Papanikolopoulos, and B. Mettler, “Autonomous altitude estimation of a UAV using a single onboard camera,” in *2009 IEEE/RSJ International Conference on Intelligent Robots and Systems*, 2009, pp. 3900–3905.
- [10] I. S. G. Campos, E. R. Nascimento, G. M. Freitas, and L. Chaimowicz, “A height estimation approach for terrain following flights from monocular vision,” *Sensors*, vol. 16, no. 12, 2016.
- [11] D. Eynard, P. Vasseur, C. Demonceaux, and V. Frémont, “UAV altitude estimation by mixed stereoscopic vision,” in *2010 IEEE/RSJ International Conference on Intelligent Robots and Systems*, 2010, pp. 646–651.
- [12] B. Herisse, F.-X. Russotto, T. Hamel, and R. Mahony, “Hovering flight and vertical landing control of a VTOL unmanned aerial vehicle using optical flow,” in *2008 IEEE/RSJ International Conference on Intelligent Robots and Systems*, 2008, pp. 801–806.
- [13] A. E. Arık, “Vision-based UAV altitude estimation using deep learning: A ResNet50 approach on nadir images,” *Academic Platform Journal of Engineering and Smart Systems*, vol. 14, pp. 46–54, 2026.
- [14] Y. Ye, S. Chen, K. Wang, X. Song, J. Dang, Q. Yu, X. Teng, and Z. Li, “Scale-Aware UAV-to-Satellite Cross-View Geo-Localization: A Semantic Geometric Approach,” *arXiv e-prints*, Mar. 2026.
- [15] L. Yang, B. Kang, Z. Huang, Z. Zhao, X. Xu, J. Feng, and H. Zhao, “Depth anything V2,” in *Advances in Neural Information Processing Systems*, A. Globerson, L. Mackey, D. Belgrave, A. Fan, U. Paquet, J. Tomczak, and C. Zhang, Eds., vol. 37. Curran Associates, Inc., 2024, pp. 21 875–21 911.
- [16] L. Piccinelli, C. Sakaridis, Y.-H. Yang, M. Segu, S. Li, W. Abbeloos, and L. Van Gool, “UniDepthV2: Universal Monocular Metric Depth Estimation Made Simpler,” *arXiv e-prints*, Feb. 2025.
- [17] S. Lin, Z. Zhang, Z. Huang, Y. Lu, C. Lan, P. Chu, Q. You, J. Wang, Z. Liu, A. Parulkar, V. Navkal, and Z. Chen, “Deep frequency filtering for domain generalization,” in *2023 IEEE/CVF Conference on Computer Vision and Pattern Recognition (CVPR)*, 2023, pp. 11 797–11 807.
- [18] Y. Yang and S. Soatto, “FDA: Fourier domain adaptation for semantic segmentation,” in *2020 IEEE/CVF Conference on Computer Vision and Pattern Recognition (CVPR)*, 2020, pp. 4084–4094.
- [19] L. Stewart, F. Bach, Q. Berthet, and J.-P. Vert, “Regression as Classification: Influence of task formulation on neural network features,” in *Proceedings of The 26th International Conference on Artificial Intelligence and Statistics*, ser. Proceedings of Machine Learning Research, F. Ruiz, J. Dy, and J.-W. van de Meent, Eds., vol. 206. PMLR, 25–27 Apr 2023, pp. 11 563–11 582.
- [20] R. Díaz and A. Marathe, “Soft labels for ordinal regression,” in *2019 IEEE/CVF Conference on Computer Vision and Pattern Recognition (CVPR)*, 2019, pp. 4733–4742.
- [21] H. Fu, M. Gong, C. Wang, K. Batmanghelich, and D. Tao, “Deep ordinal regression network for monocular depth estimation,” in *2018 IEEE/CVF Conference on Computer Vision and Pattern Recognition*, 2018, pp. 2002–2011.
- [22] M. Kim, A. K. Jain, and X. Liu, “AdaFace: Quality adaptive margin for face recognition,” in *2022 IEEE/CVF Conference on Computer Vision and Pattern Recognition (CVPR)*, 2022, pp. 18 729–18 738.
- [23] M. Tan and Q. Le, “EfficientNet: Rethinking model scaling for convolutional neural networks,” in *Proceedings of the 36th International Conference on Machine Learning*, ser. Proceedings of Machine Learning Research, K. Chaudhuri and R. Salakhutdinov, Eds., vol. 97. PMLR, 09–15 Jun 2019, pp. 6105–6114.
- [24] J. Johnson, M. Douze, and H. Jégou, “Billion-scale similarity search with GPUs,” *IEEE Transactions on Big Data*, vol. 7, no. 3, pp. 535–547, 2021.
- [25] R. Zhu, L. Yin, M. Yang, F. Wu, Y. Yang, and W. Hu, “SUES-200: A multi-height multi-scene cross-view image benchmark across drone and satellite,” *IEEE Transactions on Circuits and Systems for Video Technology*, vol. 33, no. 9, pp. 4825–4839, 2023.
- [26] M. Dai, E. Zheng, Z. Feng, L. Qi, J. Zhuang, and W. Yang, “Vision-based UAV self-positioning in low-altitude urban environments,” *IEEE Transactions on Image Processing*, vol. 33, pp. 493–508, 2024.
- [27] Z. Zheng, Y. Wei, and Y. Yang, “University-1652: A multi-view multi-source benchmark for drone-based geo-localization,” in *Proceedings of the 28th ACM International Conference on Multimedia*, ser. MM ’20. New York, NY, USA: Association for Computing Machinery, 2020, pp. 1395–1403.
- [28] W. Xu, Y. Yao, J. Cao, Z. Wei, C. Liu, J. Wang, and M. Peng, “UAV-VisLoc: A Large-scale Dataset for UAV Visual Localization,” *arXiv e-prints*, May 2024.
- [29] S. Dodge and L. Karam, “Understanding how image quality affects deep neural networks,” in *2016 Eighth International Conference on Quality of Multimedia Experience (QoMEX)*, 2016, pp. 1–6.
- [30] F. Lu, X. Lan, L. Zhang, D. Jiang, Y. Wang, and C. Yuan, “CricaVPR: Cross-image correlation-aware representation learning for visual place recognition,” in *2024 IEEE/CVF Conference on Computer Vision and Pattern Recognition (CVPR)*, 2024, pp. 16 772–16 782.
- [31] S. Izquierdo and J. Civera, “Optimal transport aggregation for visual place recognition,” in *2024 IEEE/CVF Conference on Computer Vision and Pattern Recognition (CVPR)*, 2024, pp. 17 658–17 668.
- [32] M. Oquab, T. Darcet, T. Moutakanni, H. V. Vo, M. Szafraniec, V. Khalidov, P. Fernandez, D. HAZIZA, F. Massa, A. El-Nouby, M. Assran, N. Ballas, W. Galuba, R. Howes, P.-Y. Huang, S.-W. Li, I. Misra, M. Rabbat, V. Sharma, G. Synnaeve, H. Xu, H. Jegou, J. Mairal, P. Labatut, A. Joulin, and P. Bojanowski, “DINOv2: Learning robust visual features without supervision,” *Transactions on Machine Learning Research*, 2024.
- [33] B. E. Boser, I. M. Guyon, and V. N. Vapnik, “A training algorithm for optimal margin classifiers,” in *Proceedings of the Fifth Annual Workshop on Computational Learning Theory*, ser. COLT ’92. New York, NY, USA: Association for Computing Machinery, 1992, pp. 144–152.
- [34] B. Schölkopf, J. C. Platt, J. C. Shawe-Taylor, A. J. Smola, and R. C. Williamson, “Estimating the support of a high-dimensional distribution,” *Neural Comput.*, vol. 13, no. 7, pp. 1443–1471, Jul. 2001.
- [35] E. Müller-Budack, K. Pustularen, and R. Ewerth, “Geolocation estimation of photos using a hierarchical model and scene classification,” in *Computer Vision – ECCV 2018*, V. Ferrari, M. Hebert, C. Sminchisescu, and Y. Weiss, Eds. Cham: Springer International Publishing, 2018, pp. 575–592.
- [36] J. Shang, Y. Liu, Y. Xu, J. Xiao, and D. Ma, “Robust global localization for urban autonomous vehicles via 3D geometric-enhanced visual place recognition,” *IEEE Transactions on Intelligent Transportation Systems*, vol. 26, no. 11, pp. 18 553–18 567, 2025.
- [37] W. Ma, S. Huang, and Y. Sun, “SkyLoc: Cross-modal global localization with a sky-looking fish-eye camera and OpenStreetMap,” *IEEE Transactions on Intelligent Transportation Systems*, vol. 26, no. 5, pp. 5832–5842, 2025.